Analyst

ROYAL SOCIETY OF CHEMISTRY

PAPER

View Article Online
View Journal | View Issue

Cite this: *Analyst*, 2022, **147**, 4578

A DNA tetrahedral nanomaterial-based dual-signal ratiometric electrochemical aptasensor for the detection of ochratoxin A in corn kernel samples†

Yu-Long Li, Fa-Ting Xie, Cao Yao, Gui-Qun Zhang, Yan Guan, Yun-Hui Yang, Jian-Mei Yang* and Rong Hu *

Ochratoxin A (OTA) is a highly toxic food contaminant and is harmful to human beings. Herein, a ratiometric electrochemical aptasensor based on a DNA tetrahedral nanomaterial (NTH) was developed in combination with the signal tag of a zirconium metal–organic framework (UiO-66) for the detection of OTA. In the sensor, UiO-66 and a $[Fe(CN)_6]^{3-/4-}$ electrolyte solution were used as the signal probe and the internal reference probe, respectively. In the presence of OTA, the OTA aptamer was released from the electrode due to the specific binding of OTA. Thus, signal probe P1 labeled-UiO-66 was captured on the electrode surface by hybridization with DNA NTH. Since signal probe P1 labeled-UiO-66 was close to the electrode, it leads to an increased signal current of UiO-66 at +0.9 V. As the conductivity of the modified electrode decreased, the current signal of $[Fe(CN)_6]^{3-/4-}$ at +0.2 V also decreased. The proposed ratiometric electrochemical aptasensor could effectively eliminate external environmental influences and could avoid electrochemical background signals. The aptasensor demonstrated high specificity for OTA, and achieved a good linear range of 1 pg mL^{-1}–100 ng mL^{-1} with a detection limit of 330 fg mL^{-1}. The developed electrochemical aptamer biosensor effectively detected OTA in corn kernel samples, verifying its practical application for the determination of OTA in actual samples.

Received 6th June 2022,
Accepted 17th July 2022

DOI: 10.1039/d2an00934j

rsc.li/analyst

1. Introduction

Ochratoxin A (OTA) is a kind of mycotoxin mainly produced by *Aspergillus* and *Penicillium*.[1,2] OTA is highly toxic and widely distributed in a broad array of agricultural commodities globally, including wheat, corn, rice, coffee, peanuts, legumes, and vegetables and their processed products such as wine, beer, animal feed, and vegetable oils.[3,4] Eventually, its spread through the food chain causes harm to animals and humans, especially, nephrotoxicity, hepatotoxicity, mutagenicity, and immunosuppression.[5,6] Moreover, OTA has also been categorized by the IARC (International Agency for Research on Cancer) as a possible human carcinogen (Group 2B).[7] Considering the ubiquitous presence of OTA as an ultra-low residue in edible foods along with its potential to cause high morbidity and severe toxicity, the development of a rapid and sensitive strategy for OTA detection is currently needed to avoid the risk of OTA consumption and to ensure food safety.

The current analytical methods to detect OTA include enzyme-linked immunosorbent assay (ELISA),[8] thin-layer chromatography (TLC),[9] surface-enhanced Raman scattering (SERS),[10] and fluorescence analysis.[11] Besides having advantages, these methods are limited by expensive and laborious processes, costly equipment, or proneness to false-positive results. To overcome such limitations of traditional analytical techniques, various sensors have been proposed to detect OTA.[12,13] Among them, electrochemical aptasensors are widely used due to their low cost, low detection limit, rapid analysis and portability.[14–16] Aptamers are single-stranded DNA or RNA oligonucleotides with specific binding to various biomolecules, and have the unique advantages of simple synthesis, easy storage, high selectivity and affinity over antibodies. They are very suitable to be used as biorecognition elements for the detection of OTA.[17–19] To date, most electrochemical aptasensors mainly rely on a single response signal to quantify OTA analytes. Although the experimental procedures of these methods are simple and easy to detect, some environmental conditions and operational factors may affect the detection results.[20,21] To address this problem, the combination of a ratiometric strategy with an electrochemical sensor

College of Chemistry and Chemical Engineering, Yunnan Normal University, Kunming, 650500, P. R. China. E-mail: hudierong_168@163.com, yangatynnu@163.com; Tel: +86-871-65149087

†Electronic supplementary information (ESI) available: Additional experiment data, Fig. (S1–S4) and Tables (S1–S4). See DOI: https://doi.org/10.1039/d2an00934j

has been considered a feasible approach.[22,23] Ratiometric electrochemical sensors quantitatively analyze the target by using the ratio of two signals (the ratio of non-absolute values) and effectively eliminate the environmental interference by exploiting a built-in calibration function. Hence, the reliability and accuracy of the analysis are improved.[24,25]

Metal–organic frameworks (MOFs) are ordered network structures formed by the combination of organic bridging ligands and inorganic metal ions.[26] Numerous studies have demonstrated significant advantages of MOFs in sensing,[27] gas storage,[28] and catalysis[29] ascribed to their porous structure and large specific surface area. However, many MOFs suffer from various instabilities, which can be overcome by combining MOFs with metal (Ag, Au, *etc.*) nanoparticles (NPs).[30,31] The present work employed zirconium (Zr) MOFs, *viz.* UiO-66, as the signal label and the results showed that the MOFs could show an excellent electrochemical activity. The electrochemical current signal of UiO-66 was strong, stable, and detectable without the procedure of acid dissolution and preconcentration.

To obtain a stable electrochemical aptamer biosensor, it is essential to assemble a stable substrate on the electrode surface. For instance, tetrahedral and other DNA nanostructures are often assembled on the electrode surface through one-step thermal denaturation.[32,33] Among them, the DNA nanotetrahedron (NTH) with a spatial structure has a stable and rigid structure that can precisely locate the orientation of the probe and obliterate the non-specific binding of DNA and target on the substrate.[34,35] Ultimately, 3D DNA NTH facilitates the efficient recognition of the target to improve the precision and accuracy of the detection method.[36] The electrical conductivity of sensing platforms can be improved by exploiting MXene materials, which are characterized by the convenience of functionalization, hydrophilicity, and high electrical conductivity and capacity.[37,38] The electrical conductivity of MXene materials can be further tuned by embedding them with noble metal nanoparticles, such as gold (Au) and silver (Ag).[39] Furthermore, the thiol group (–SH) at the bottom of DNA NTH can be stably connected to MXene through the Au–S bond. Therefore, the combination of Au NPs@MXene and DNA NTH could be significant to develop a biosensing platform with high sensitivity and stability.

In the proposed strategy, a ratiometric electrochemical aptasensor was designed by exploiting UiO-66 as signal tags and MXene as a sensing platform for the determination of OTA (Scheme 1). MXene enhanced the immobilization amount of DNA NTH, and the use of aptamer-incorporated DNA NTH as a recognition element enabled higher accessibility and control over spatial orientation. We employed UiO-66 as the signal probe (UiO-66-SP) and $K_3Fe(CN)_6/K_4Fe(CN)_6$ in the electrolyte solution as the internal reference probe ($[Fe(CN)_6]^{3-/4-}$-IR). In the presence of the target OTA, the OTA aptamer specifically bound to OTA and subsequently dissociated from the DNA NTA tip. The signal probe of strand DNA P1 could be bound to the top of DNA NTH; thus, the increased current signal of

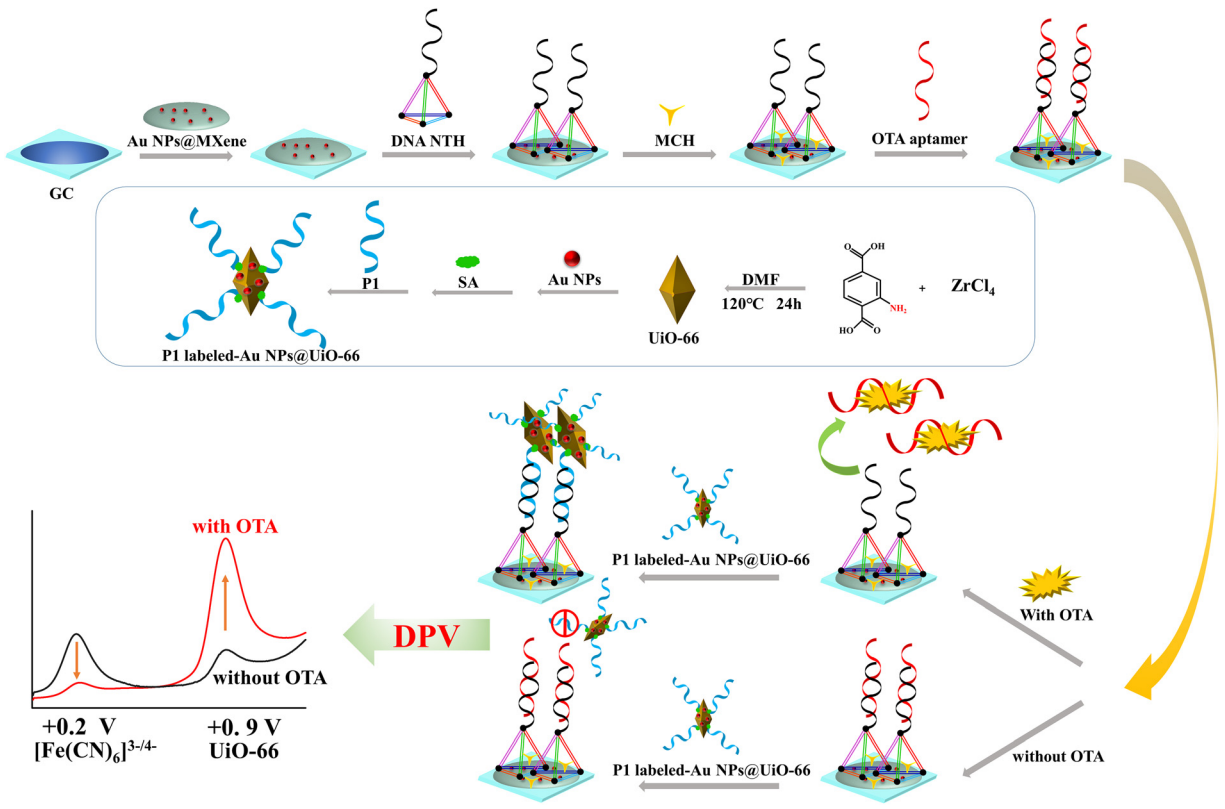

Scheme 1 Fabrication and detection principle of the electrochemical aptamer biosensor for OTA detection.

UiO-66 could be detected by differential pulse voltammetry (DPV), while the current of $K_3Fe(CN)_6/K_4Fe(CN)_6$ as the internal reference probe was decreased. Thus, the ratio response of $I_{UiO\text{-}66\text{-}SP}/I_{[Fe(CN)_6]^{3-/4-}\text{-}IR}$ was adopted for the quantitative analysis of OTA. The limit of detection (LOD) was obtained as 330 fg mL^{-1}. These results highlighted the potential of the developed electrochemical aptasensor as a simple, sensitive, economical, fast, and stable system with a low LOD for the determination of OTA in corn kernel samples. The results were also aligned to those achieved from commercial ELISA.

2. Experimental section

2.1 Materials and apparatus

Zirconium chloride ($ZrCl_4$) and 2-aminoterephthalic acid were obtained from McLean Reagent Co., Ltd (Shanghai, China). OTA was provided by Sigma-Aldrich (USA). Corn kernels were purchased from a local Walmart supermarket (Yunnan, China). MXene was obtained from Forsman Technology Beijing Co., Ltd (Beijing, China). DNA sequences were supplied by Sangon Biotech Co., Ltd (Shanghai, China) (see Table S1 in the ESI† for sequences).

Electrochemical experiments, including cyclic voltammetry (CV), electrochemical impedance spectroscopy (EIS) and differential pulse voltammetry (DPV), were carried out on a CHI650E workstation (CHI Instruments Inc., Chenhua Corp., China) by using a conventional three-electrode system with a glassy carbon (GC) electrode as the working electrode, platinum wire as the auxiliary electrode and a saturated calomel electrode as the reference electrode. CV and EIS experiments were performed in 0.1 M KCl solution containing 5 mM $[Fe(CN)_6]^{3-/4-}$. DPV experiments were conducted in Tris-HCl buffer (pH 7.4) containing 0.25 mM $K_3Fe(CN)_6/K_4Fe(CN)_6$. The sweep range was from 0 V to 1.2 V with a pulse amplitude of 0.05 V and a pulse period of 0.2 s.

Transmission electron microscopy (TEM) images were taken using a JEM 2100 (Nippon Electronics Co., Ltd Japan). X-ray diffraction (XRD) spectra were measured using a TTRIII (Nippon Science Corporation, Japan). X-ray photoelectron spectroscopy (XPS) was performed on a K-Alpha+ (Thermo Fisher Scientific, USA). Infrared (IR) spectra were measured using an iS10 (Nicholas, USA).

2.2. Preparation of DNA NTH

The four strands of DNA NTH were connected by annealing. Tetra-OTA, Tetra X, Tetra-Y, and Tetra-Z were first centrifuged for 1 min and then dissolved in a buffer solution (pH 8.0, 10 mM Tris-HCl and 25 mM $MgCl_2$). Next, the four DNA strands were mixed, annealed at 100 °C for 3 minutes, and finally placed at 4 °C. The final concentration is 2.5 μM.

2.3 Synthesis of Au NPs

Au NPs were prepared according to the previously reported literature.[40] Briefly, 100 mL of water and 1 mL of $HAuCl_4{\cdot}4H_2O$ (1 w%) were heated with stirring in a reaction vessel. When the solution boiled, 3.5 mL of trisodium citrate (1 w%) solution was quickly poured. After reacting for a while, when the mixtures turned wine red, they were cooled to room temperature and the obtained Au NPs were stored at 4 °C.

2.4 Synthesis of Au NPs@UiO-66

UiO-66 was synthesized by following the method reported in the literature.[41] In short, weighed amounts of $ZrCl_4$ (0.0543 g) and 2-aminoterephthalic acid (0.0422 g) were mixed in 3 mL of DMF. Following ultrasonication for 0.5 h, the mixture was allowed to react for 24 h at 120 °C. The resulting solution was refluxed with DMF at 50 °C for 20 h. Finally, the obtained precipitate was washed with DMF and absolute ethanol several times, dried at 80 °C, and stored after sealing.

Next, Au NPs were slowly dropped in a dispersion of UiO-66 (50 mg) in water (25 mL) under continuous stirring for 20 h. After centrifugation at 5000 rpm, the precipitate was washed thrice with water, dried under vacuum at 60 °C, and stored for further use.

2.5 Signal probe P1-labeled Au NPs@UiO-66

A dispersion of 20 mg of the Au NPs@UiO-66 complex in 500 μL of water was reacted with EDC (200 mM, 400 μL) and NHS (200 mM, 400 μL) for 30 min. After centrifugation, the precipitate was dispersed in 300 μL of water in which 100 μL of streptavidin (SA, 1 mg L^{-1}) was subsequently added and shaken for 5 h at 4 °C. With the help of EDC and NHS activators, the amino group of Au NPs@UiO-66 can be combined with the carboxyl group of SA to form SA modified Au NPs@UiO-66. Subsequently, 250 μL of P1 (10 μM) was added to the above mixture and reacted for 2 h. After that, 1 mL of 2-mercaptoethanol (MCH, 10%) was added and reacted at 4 °C for 30 minutes. Finally, the mixed solution was centrifuged at 10 000 rpm and the obtained precipitate was washed twice with buffer, dissolved with 500 μL of water, and stored at 4 °C. The final concentration is 0.04 mg mL^{-1}.

2.6 Synthesis of Au NPs@MXene

20 mg of MXene was first dispersed in 50 mL of water; then 600 μL of $HAuCl_4{\cdot}4H_2O$ (1 w%) was added to the dispersion and stirred for 20 min. After centrifugation at 5000 rpm for 20 min, the precipitate was vacuum-dried and the as-obtained Au NPs@MXene was dispersed in water at a concentration of 5 mg mL^{-1} for further use.[42]

2.7 Preparation of corn sample solution

First, 5 g of corn granules were weighed and dissolved in 10 mL of methanol solution (90% v/v). Then, the mixture was sealed and stirred at room temperature for 30 min. Next, the mixture was filtered through a filter membrane with a pore size of 0.22 μm. The collected filtrate was diluted with distilled water at a ratio of 1 : 20, and stored at 4 °C for later use.

2.8 Preparation and measurement of aptamer sensors

The GC electrodes were first polished with 1.5 μm, 0.5 μm, and 50 nm alumina slurries, respectively, and then ultrasonically

treated with HNO_3, ethanol, and water in sequence.[43] Next, 10 μL of Au NPs@MXene (5 mg mL^{-1}) mixed with chitosan solution at a ratio of 1 : 1 was dropped on the electrode and dried. After that, the electrode was incubated with 10 μL of DNA NTH (2.5 μM) at 37 °C overnight. Subsequently, the resulting electrode was blocked with 1% MCH for 10 min and rinsed with buffer. Then, 10 μL of OTA aptamer (2.5 μM) was placed onto the electrode surface for reaction for 2 h at 37 °C. Afterward, the electrode was further incubated with 10 μL of OTA at 37 °C for 2 h. Finally, 10 μL of P1 labeled-Au NPs@UiO-66 (0.04 mg mL^{-1}) was added to the modified electrode for 1 h. The desired sensor was produced.

3. Results and discussion

3.1. Design strategy

Scheme 1 shows the principle of the proposed ratiometric electrochemical aptasensor. The terminal of DNA NTH could hybrid with OTA aptamers or P1. The decoration of Au NPs@MXene onto the GC electrode was followed by the assembling of DNA NTH to form the stable substrate. OTA aptamers were then hybridized with the terminal of DNA NTH. At this point, P1 could not approach DNA NTH. The highly specific binding of OTA could enable the release of OTA aptamers. Thus, the signal tag P1 labeled-UiO-66 was immobilized by hybridization with the tip of DNA NTH. Being close to the electrode, signal probe P1 labeled-UiO-66 led to an increased signal current of UiO-66 at +0.9 V. On the other hand, a decrease in the conductivity of the modified electrode was associated with a reduction in the current signal of $K_3Fe(CN)_6$/$K_4Fe(CN)_6$ at +0.2 V. Therefore, a ratiometric electrochemical aptasensor was successfully constructed for the detection of OTA.

The feasibility of the experimental design was verified through a series of control experiments. Upon the addition of P1 labeled-UiO-66, Fig. 1A shows a low electrochemical signal of UiO-66 at +0.9 V in the absence of Tetra-OTA (curve a) or OTA (curve b). The current signal of $K_3Fe(CN)_6$/$K_4Fe(CN)_6$ as the internal reference probe was relatively high. Contrarily, when OTA aptamer/Tetra-OTA/OTA were both present (curve c), the detected electrochemical signal for UiO-66 increased, while the current signal of $K_3Fe(CN)_6$/$K_4Fe(CN)_6$ decreased. In the absence of the OTA aptamer, P1 labeled-UiO-66 could directly bind with the terminal of DNA NTH. Therefore, a phenomenon (curve d) slightly higher than the curve c was observed. These control experiments thereby validated the feasibility of the experimental scheme. Fig. 1B is a histogram of the results of control experiments highlighting the experimental convenience for more intuitive observation. In order to further verify the advantages of designed DNA NTH, single-stranded DNA Tetra OTA 2 (without forming DNA NTH structures, the Tetra OTA 2 sequence is detailed in Table S1†) was designed. Compared with DNA NTH, from Fig. S1,† it can be seen that the gap between the target and the blank obtained by DNA NTH was larger than that of the single-stranded DNA Tetra OTA. Because

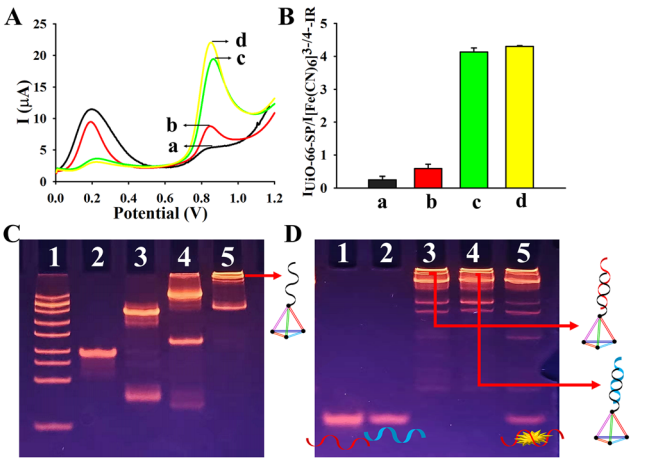

Fig. 1 (A) Curves and (B) histogram of DPV responses under different experimental conditions. (a: Tetra X + Tetra Y + Tetra Z + OTA + OTA aptamer; b: Tetra OTA + Tetra X + Tetra Y + Tetra Z + OTA aptamer; c: Tetra OTA + Tetra X + Tetra Y + Tetra Z + OTA + OTA aptamer; d: Tetra OTA + Tetra X + Tetra Y + Tetra Z + OTA). (C) PAGE electropherogram of DNA marker (band 1), Tetra OTA (band 2), Tetra OTA + Tetra X (band 3), Tetra OTA + Tetra X + Tetra Y (band 4), and Tetra OTA + Tetra X + Tetra Y + Tetra Z (band 5). (D) PAGE electropherogram of OTA aptamer (band 1), P1 (band 2), DNA NTH + OTA aptamer (band 3), DNA NTH + P1 (band 4), and DNA NTH + OTA aptamer + OTA (band 5).

DNA NTH can reduce the non-specific binding on the substrate, and it can also facilitate the efficient recognition of the target.

The DNA assembly process was verified by polyacrylamide gel electrophoresis (PAGE) experiments. DNA NTH was constructed by the self-assembly of four DNA strands (Tetra OTA, Tetra X, Tetra Y and Tetra Z). In Fig. 1C, band 1 represents the DNA marker (25–500 bp) while band 2 indicates the fast migration rate of the single-stranded Tetra OTA. The slower migration of band 3 than that of band 2 and the slower migration of band 4 than that of band 3 could be ascribed to the movement of DNA hindered by the increase of space complexity and molecular weight. When the four single strands were hybridized together, the lowest mobility in band 5 was observed. The obvious difference in the band positions indicated the successful synthesis of DNA NTH. The formation of DNA NTH was further observed by transmission electron microscopy, and a large number of DNA NTH nanoparticles could be seen (Fig. S2†). Regarding the assembly results (Fig. 1D), band 1 and band 2 with much fast migration rates correspond to the single nucleotide OTA aptamer and P1, respectively, whereas band 3 represents the hybridization of the OTA aptamer with the DNA NTH tip. Since the increase of molecular weight could slow down the rate of DNA movement, the hybridization of P1 with DNA NTH resulted in a significantly lower migration rate of band 4 than that of band 2. The obvious difference in the band positions indicated that DNA NTH could efficiently hybridize with the OTA aptamer or P1. Furthermore, a new band at the same position of the OTA aptamer in band 5 appeared in the presence of OTA. These apparent electrophoretic characterization results indicated the successful experimental design of the present study.

3.2. Characterization of materials

The TEM analysis exhibited the octahedral morphology of UiO-66 (Fig. 2A) along with the presence of Au NPs on its surface (Fig. 2B) accentuating the successful synthesis of the Au NPs@UiO-66 composites. The XRD pattern of as-prepared UiO-66 (Fig. 2C) shows two characteristic peaks around 7.34 and 8.48, which is consistent with the literature.[41] Four main characteristic peaks in the XRD patterns of Au NPs@UiO-66 (Fig. 2C), all of which, are located on the lattice of the face-centered single cubic crystals of Au. Furthermore, the two absorption bands at 3470 cm^{-1} and 3382 cm^{-1} correspond to the asymmetric and symmetric modes of N–H stretching, respectively, while the stretching vibration of C–N corresponds to the peak at 1255 cm^{-1} (Fig. 2D). Regarding IR spectroscopy, the obtained results were overall similar to those reported by Abid *et al.*[44]

The XPS detection method can characterize the newly formed chemical bonds inside the synthesized materials. The XPS spectra of Au NPs@UiO-66 show that the sample comprised of Zr, N, O, C, and Au elements, indicating the successful preparation of Au NPs@UiO-66 complexes (Fig. 2E). The two peaks of the Zr element at 182.5 eV and 184.9 eV are characteristic peaks of Zr 3d and Zr 2p, respectively (Fig. 2F).[41] The N 1s spectrum is divided into several symmetrical peaks, of which 398.9 eV and 400.3 eV correspond to the stretching vibrations of N–C and N–H respectively (Fig. 2G).[45] The spectral peak of O 1s appeared at 531.4 eV (Fig. 2H) while the C 1s spectrum was fitted with two symmetrical component peaks at 284.3 eV and 288.2 eV respectively corresponding to the –COO– and C–C functional groups (Fig. S3†). Similarly, the Au spectrum was also divided into two peaks at 81.7 eV and 85.3 eV; the former corresponds to Au 4f7 whereas the latter is ascribed to Au 4f5 (Fig. 2I).

MXene and Au NPs@MXene were also characterized by XRD and TEM. MXene exhibited a two-dimensional layered structure (Fig. 3A) with surfaces having a uniform distribution of Au NPs (Fig. 3B). The XRD analysis results of MXene are similar to those mentioned in literature reports (Fig. 3C). The four main characteristic peaks in the XRD spectrum of Au NPs@MXene are located on the lattice of the face-centered cubic Au single crystals, and the results further prove the successful doping of Au NPs (Fig. 3C).[42]

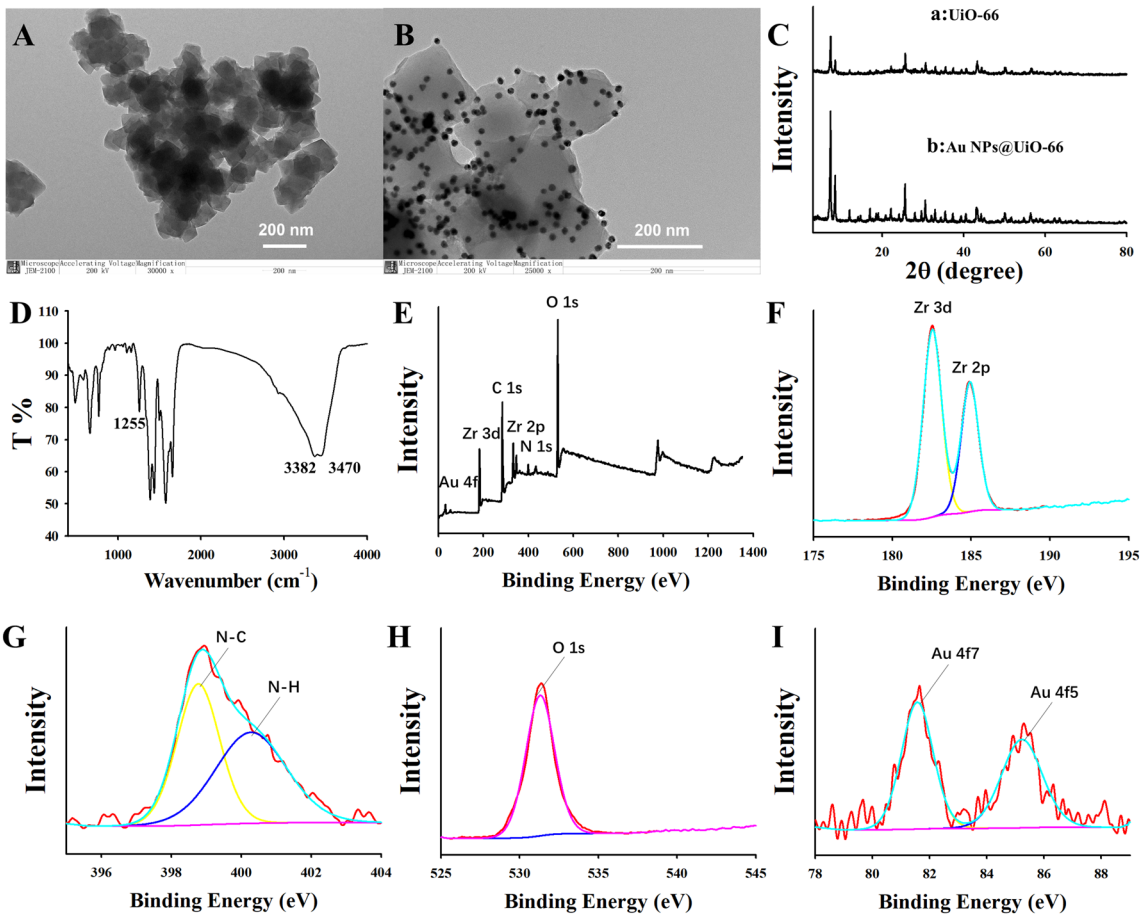

Fig. 2 TEM images of (A) UiO-66 and (B) Au NPs@UiO-66. (C) XRD patterns of UiO-66 and Au NPs@UiO-66. (D) IR spectrum of UiO-66. XPS spectra of (E) Au NPs@UiO-66, (F) Zr, (G) N 1s, (H) O 1s and (I) Au.

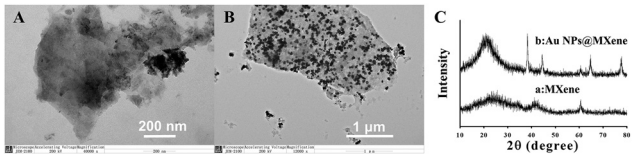

Fig. 3 TEM images of (A) MXene and (B) Au NPs@MXene. (C) XRD patterns of (a) MXene and (b) Au NPs@MXene.

3.3. Electrochemical characterization of the electrode modification process

The modified electrode and its stepwise construction were investigated by EIS and CV in a $[Fe(CN)_6]^{3-/4-}$ solution. As shown in the EIS spectra (Fig. 4A), a small semicircle was obtained for the bare GC electrode (curve a, R_{ct} = 250 Ω). After modified with Au NPs@MXene, the electrode exhibited a smaller semicircle (curve b, R_{ct} = 180 Ω) due to the excellent electrical conductivity of MXene. However, the addition of DNA NTH to the electrode led to an increase in the resistance (curve c, R_{ct} = 750 Ω) because of the electrostatic repulsion between $[Fe(CN)_6]^{3-/4-}$ and the negative charges on the phosphate backbones of DNA NTH.[46,47] Blocking the non-specific binding sites of the electrodes with MCH also resulted in a gradual increase in the R_{ct} value (curve d, R_{ct} = 940 Ω) pertaining to the hindrance caused in electron transfer by MCH. The R_{ct} value further increased following the combination of the OTA aptamer with the modified electrode surface (curve e, R_{ct} = 1700 Ω). However, the introduction of the target OTA relatively decreased the R_{ct} value (curve f, R_{ct} = 1500 Ω) owing to the dissociation of some aptamer chains. After P1 labeled-Au NPs@UiO-66 was combined with the modified electrode surface, the R_{ct} value reached the maximum (curve g, R_{ct} = 2200 Ω).

The cyclic voltammetric analysis of the assembly process on the electrode surface (Fig. 4B) exhibited redox peaks with excellent peak shape for the pristine electrode (curve a). The redox peak current of Au NPs@MXene-coated GC (curve b) was slightly higher than that of the unmodified GC electrode. Conversely, the redox peak of the DNA NTH-incubated electrode interface (curve c) decreased in relation to the Au NPs@MXene-coated electrode. Upon being blocked with MCH, the redox peak current was significantly suppressed (curve d) ascribing to the shielding effect of MCH on the active site. The redox peak current was further reduced when the modified electrode surface was bound to the OTA aptamer (curve e). As the addition of the target on the electrode surface could dissociate a part of the aptamer chain, the redox current response signal increased compared to the peak current of the OTA aptamer-bound electrode surface (curve f). When the modified electrode surface was combined with P1-labeled Au NPs@UiO-66, the redox peak current reached the lowest (curve g).

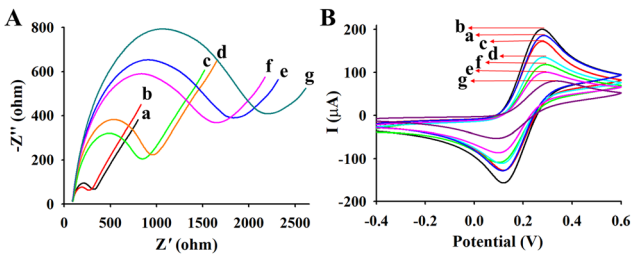

Fig. 4 (A) EIS spectra and (B) CV of different electrodes. (a: bare GC, b: Au NPs@MXene/GC, c: DNA NTH/Au NPs@MXene/GC, d: MCH/DNA NTH/Au NPs@MXene/GC, e: OTA aptamer/MCH/DNA NTH/Au NPs@MXene/GC, f: OTA/OTA aptamer/MCH/DNA NTH/Au NPs @MXene/GC, g: OTA/OTA aptamer/MCH/DNA NTH/Au NPs @MXene/GC/P1 labeled-Au NPs@UiO-66).

The excellent conductivity of Au NPs combined with the large specific surface area of the MXene film caused the largest peak current of Au NPs@MXene/GC among all the modified electrodes. The effective surface areas were calculated using the Randles–Sevcik equation:

$$I_p = 2.69 \times 10^5 n^{3/2} A D^{1/2} \nu^{1/2} C \quad (1)$$

where I_p is the peak current, n is the number of electrons referring to the redox reaction process (= 1), D represents the diffusion coefficient (6.7×10^{-6} cm^2 s^{-1}), ν is the scan rate (0.1 V s^{-1}), and C stands for the concentration of the probe molecule in the solution (2.5×10^{-6} mol cm^{-3}). The calculated effective surface areas (A) of bare GC and Au NPs@MXene/GC were 0.2694 and 0.3141 cm^2, respectively. Thus, the Au NPs@MXene/GC caused a 1.15-fold increase in the electroactive surface area of the unmodified bare GC.

3.4. Optimization of the experimental conditions

The measurement conditions including the pH of buffer and the incubation time of P1 labeled-Au NPs@UiO-66 were optimized and the results are presented in Fig. S4A† which shows an increase in the sensor response signal ratio with increasing incubation time of UiO-66-SP. At an incubation time over 60 min, the ratio of the current response remained stable implying that the basic assembly of UiO-66-SP was completed within 60 min. The effect of the pH of buffer on the sensitivity of the system was further investigated. As displayed in Fig. S4B,† the response-to-signal ratio gradually enhanced with the increase of pH and reached a maximum at pH 7.5. Therefore, the pH was chosen 7.5 in the further experiments.

3.5. Response performance of the sensors to OTA

The dual signal ratiometric electrochemical aptasensor was then used for OTA detection at different concentrations, demonstrating the potential of the proposed sensor in quantifying analytes. Fig. 5A demonstrates the DPV current responses of the biosensor to OTA at various concentrations. With the increase of the OTA concentration, more signal probe UiO-66 materials were captured on the electrode surface, so the peak current of UiO-66-SP gradually intensified, while that of $[Fe(CN)_6]^{3-/4-}$-IR gradually decreased. In addition, it can be observed from Fig. 5B that the current response ratio $I_{UiO\text{-}66\text{-}SP}/I_{[Fe(CN)_6]^{3-/4-}\text{-}IR}$ has a good relationship with the OTA concentration in the range of 0.001–100 ng mL^{-1}. The obtained linear

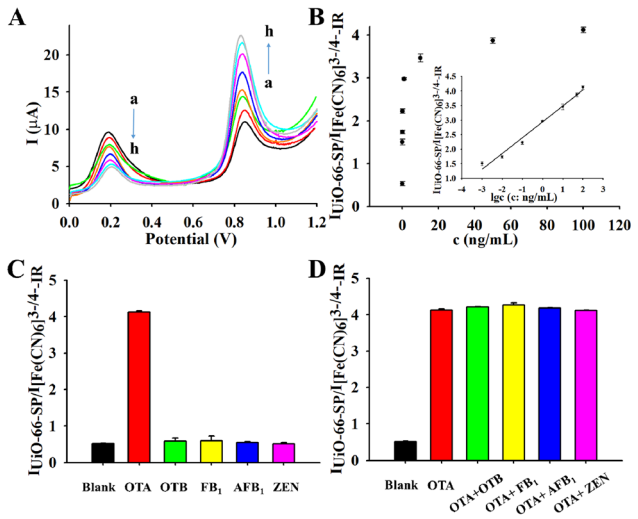

Fig. 5 (A) DPV response curve of the sensor to various concentrations of OTA (a to h: 0, 1 pg mL^{-1}, 10 pg mL^{-1}, 100 pg mL^{-1}, 1 ng mL^{-1}, 10 ng mL^{-1}, 50 ng mL^{-1}, and 100 ng mL^{-1}). (B) The current response ratio value was increased with the enhancement of OTA concentrations. The inset shows the relationship between the current response ratio and the logarithmic value of different OTA concentrations. (C) Specificity and (D) anti-interference of sensors.

equation for OTA detection is $I_{UiO-66-SP}/I_{[Fe(CN)_6]^{3-/4-}IR}$ = 0.54lgc + 2.94 (R^2 = 0.9859) with a LOD of 330 fg mL^{-1} by the 3σ rule. More importantly, it is noteworthy that the detection performance of the proposed sensor is more sensitive than those of the previously reported OTA detection methods (Table 1).

3.6. Evaluation of sensor specificity and anti-interference

Since the specificity and anti-interference are essential factors in evaluating a biosensor, the present study employed ochratoxin B (OTB), fumonisin B_1 (FB_1), aflatoxin B_1 (AFB_1), and zearalenone (ZEN) to assess the specificity of the proposed ratiometric electrochemical aptasensor. Fig. 5C demonstrates that despite a substantially higher concentration (10-fold) of the interfering substances (1000 ng mL^{-1}) than that of OTA (100 ng mL^{-1}), their response current ratio was considerably smaller than that of OTA. This pattern of the response current ratio persisted even when the interfering substances and OTA were mixed in equal amounts to the final concentration comprising 10-times more interfering substances than OTA (Fig. 5D). These results indicate only a negligible impact of the interfering substances on the target detection highlighting the good specificity and anti-interference properties of the proposed ratio sensor.

Table 1 Performance comparison of different strategies for the detection of OTA

Method sample	Linear range	LOD	Ref.
SERS	1–1000 pg mL^{-1}	0.61 pg mL^{-1}	48
SERS	0.01–50 ng mL^{-1}	8.6 pg mL^{-1}	49
Colorimetric	0.05–2.0 ng mL^{-1}	0.023 ng mL^{-1}	50
Colorimetric	10–100 mg mL^{-1}	1.15 ng mL^{-1}	51
Chemiluminescence	0.0001–1 ng mL^{-1}	0.4 pg mL^{-1}	52
Chemiluminescence	0.01–20 ng mL^{-1}	0.041 ng mL^{-1}	53
Electrochemical	0.002–6 ng mL^{-1}	0.002 ng mL^{-1}	17
Electrochemical	0.05–50 ng mL^{-1}	0.017 ng mL^{-1}	54
Electrochemical	0.05–100 ng mL^{-1}	10 pg mL^{-1}	43
Electrochemical	0.001–100 ng mL^{-1}	330 fg mL^{-1}	This work

3.7. Reproducibility of the sensor

The higher stability and accuracy of the ratiometric electrochemical sensor were confirmed by evaluating the stability of the sensor. Repeat the experiment with ten electrodes, then measure to obtain 20 sets of data. The results show that the response of the non-ratiometric sensor fluctuated widely, with an average value of 10.66 μA and an RSD of 43.85% (Fig. 6A). However, the amplitude of fluctuation reduced significantly in our designed ratiometric electrochemical sensor which exhibited an RSD of 3.71%, and an average value of 4.09 (Fig. 6B). Ratio-based strategies are more reliable than non-ratiometric methods, are characterized by high stability (Table S2†), and therefore result in more accurate data by reducing background interference and random errors.

3.8. Determination of the recovery rate and comparison with commercial enzyme-linked immunosorbent assay (ELISA)

We employed the standard addition method to test the method accuracy and reliability of the ratiometric electrochemical aptasensor by adding three levels of OTA standard solutions (5.0, 0.5, 0.005 ng mL^{-1}). The results demonstrated the recoveries ranging from 93.2% to 107.1% (Table S3†). These results show that the proposed ratiometric biosensor is suitable for real sample detection.

The detection reliability of the sensor was investigated and compared with that of a commercial ELISA kit. Fig. 6C displays that with the increase in the concentrations of OTA, the absorbance increased accordingly. The linear equation was y = 0.0611x + 0.1617 (R^2 = 0.991) in the range from 0.625 to 20 ng

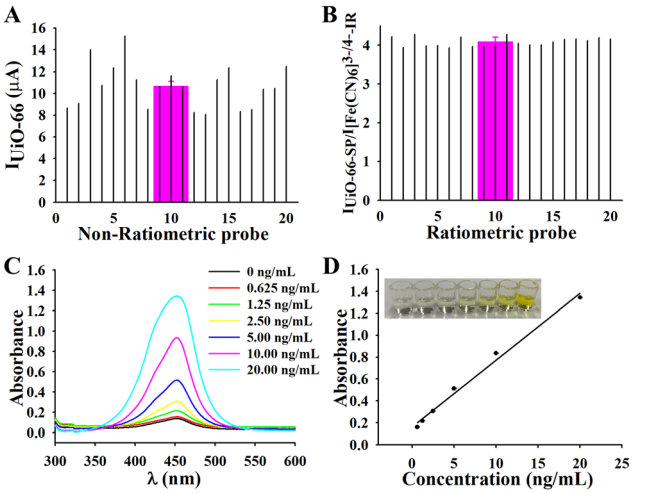

Fig. 6 Comparison of reproducibility between (A) non-ratiometric sensor and (B) ratiometric sensor. (C) UV absorption spectrum and (D) calibration curve of the ELISA kit for different concentrations of OTA.

Table 2 Comparison of OTA detection with an ELISA kit in corn samples

Detection method	OTA detected (ng mL^{-1})	Average (ng mL^{-1})	RSD (%)
ELISA kits	5.82 5.88 5.90	5.87	0.71
This work	5.56 5.67 5.61	5.61	0.98

mL^{-1} (Fig. 6D). It was found that the sensitivity of our strategy was 4 orders higher than that of ELISA kits. Additionally, the real corn samples were measured thrice in parallel with an ELISA kit and the developed sensor. As evident from the results in Table 2, the developed sensor has the same high accuracy as that of the commercial ELISA kit. To further verify the applicability of the sensor, other crop samples including peanut and melon seeds were also selected for OTA detection. As shown in Table S4,† our developed sensor obtained results were consistent with commercial kits.

4. Conclusions

An ultrasensitive ratiometric electrochemical aptamer biosensor for the quantitative analysis of OTA was developed by assembling DNA NTH on the working electrode and by the recognition of OTA with OTA nucleic acid aptamers. The excellent stability of well-designed tetrahedral DNA could enhance the immobilization efficiency and the electrochemical signal response, and could eventually improve the detection sensitivity. Furthermore, the ratio-based strategy was introduced which enabled the sensor to output a stable electrochemical signal and subsequently further improved the reproducibility of the detection. The detection results of OTA using the sensor were comparable to those using a commercial ELISA kit. The constructed sensor could quantitatively determine the content of OTA in real corn samples effectively in the range of 0.001–100 ng mL^{-1} with outstanding stability, superior specificity, and higher sensitivity, and with a detection limit as low as 330 fg mL^{-1}. In conclusion, the proposed electrochemical aptamer biosensor demonstrated the potential to serve as an economical, green, stable, and powerful tool for the precise detection of OTA.

Conflicts of interest

There are no conflicts to declare.

Acknowledgements

This work was financially supported by the National Natural Science Foundation of China (Grant No: 21864026 and 21605130).

References

1 Y. Wang, L. Wang, F. Wu, F. Liu, Q. Wang, X. Zhang, J. N. Selvaraj, Y. Zhao, F. Xing, W.-B. Yin, Y. Liu and H. L. Drake, *Appl. Environ. Microbiol.*, 2018, **84**, e01009–e01018.
2 L. Shang, X. Bai, C. Chen, L. Liu, M. Li, X. Xia and Y. Wang, *Food Control*, 2019, **106**, 106743.
3 V. Ostry, F. Malir and J. Ruprich, *Toxins*, 2013, **5**, 1574–1586.
4 M. Mukherjee, C. Nandhini and P. Bhatt, *Spectrochim. Acta, Part A*, 2021, **244**, 118875.
5 C. Longobardi, S. Damiano, E. Andretta, F. Prisco, V. Russo, F. Pagnini, S. Florio and R. Ciarcia, *Antioxidants*, 2021, **10**, 83.
6 Y. Wang, L. Wang, F. Liu, Q. Wang, J. N. Selvaraj, F. Xing, Y. Zhao and Y. Liu, *Toxins*, 2016, **8**, 1239.
7 A. Stefanello, A. M. Gasperini and M. V. Copetti, *Curr. Opin. Food Sci.*, 2022, **45**, 100838.
8 W. Tong, H. Fang, H. Xiong, D. Wei, Y. Leng, X. Hu, X. Huang and Y. Xiong, *Foods*, 2021, **10**, 102429.
9 I. Cabezudo, M. O. Salazar, I. Ayelen Ramallo and R. L. E. Furlan, *Food Chem.*, 2022, **8**, 132937.
10 Y. Hernández, L. K. Lagos and B. C. Galarreta, *Analyst*, 2020, **28**, 100331.
11 Y. Li, N. Zhang, H. Wang and Q. Zhao, *Analyst*, 2020, **145**, 651–655.
12 P. Wang, L. Wang, M. Ding, M. Pei and W. Guo, *Analyst*, 2019, **144**, 5866–5874.
13 X. Li, N. Falcone, M. N. Hossain, H. B. Kraatz, X. Chen and H. Huang, *Talanta*, 2021, **226**, 122183.
14 E. Cesewski and B. N. Johnson, *Biosens. Bioelectron.*, 2020, **159**, 112214.
15 J. Kudr, P. Michalek, L. Ilieva, V. Adam and O. Zitka, *TrAC, Trends Anal. Chem.*, 2021, **136**, 116192.
16 L. Lei, B. Ma, C. Xu and H. Liu, *TrAC, Trends Anal. Chem.*, 2022, **22**, 116640.
17 N. Mejri-Omrani, A. Miodek, B. Zribi, M. Marrakchi, M. Hamdi, J. L. Marty and H. Korri-Youssoufi, *Anal. Chim. Acta*, 2016, **920**, 37–46.
18 A. Y. El-Moghazy, N. Amaly, G. Istamboulie, N. Nitin and G. Sun, *Microchim. Acta*, 2020, **187**, 535.
19 T. Lin and Y. Shen, *J. Electroanal. Chem.*, 2020, **870**, 114247.
20 Y. Du, B. J. Lim, B. Li, Y. S. Jiang, J. L. Sessler and A. D. Ellington, *Anal. Chem.*, 2014, **86**, 8010–8016.
21 N. Hong, L. Cheng, B. Wei, C. Chen, L. L. He, D. Kong, J. Ceng, H. F. Cui and H. Fan, *Biosens. Bioelectron.*, 2017, **91**, 110–114.
22 R. Hu, X. Zhang, K. N. Chi, T. Yang and Y. H. Yang, *ACS Appl. Mater. Interfaces*, 2020, **12**, 30770–30778.
23 Y. An, R. Li, F. Zhang and P. He, *Talanta*, 2021, **235**, 122790.
24 Z. Liu, Y. Zhang, B. Li, X. Ren, H. Ma and Q. Wei, *Analyst*, 2020, **145**, 3320–3328.
25 C. Liu, X. Wei, X. Wang, J. Shi, Z. Chen, H. Zhang, W. Zhang and X. Zou, *Sens. Actuators, B*, 2021, **329**, 129228.

26 J. Li, X. Shan, D. Jiang and Z. Chen, *Analyst*, 2020, **145**, 3306–3312.
27 Z. Ye, Q. Wang, J. Qiao, Y. Xu and G. Li, *Analyst*, 2019, **144**, 2120–2129.
28 H. Daglar, H. C. Gulbalkan, G. Avci, G. O. Aksu, O. F. Altundal, C. Altintas, I. Erucar and S. Keskin, *Angew. Chem., Int. Ed.*, 2021, **60**, 7828–7837.
29 L. Li, Z. Li, W. Yang, Y. Huang, G. Huang, Q. Guan, Y. Dong, J. Lu, S.-H. Yu and H.-L. Jiang, *Chem*, 2021, **7**, 686–698.
30 L. Zhao, W. Wu, X. Shen, Q. Liu, Y. He, K. Song, H. Li and Z. Chen, *ACS Appl. Mater. Interfaces*, 2019, **11**, 47073–47082.
31 S. Choi, H. J. Lee and M. Oh, *Small*, 2016, **12**, 2425–2431.
32 H. Bai, S. Bu, W. Liu, C. Wang, Z. Li, Z. Hao, J. Wan and Y. Han, *Analyst*, 2020, **145**, 7340–7348.
33 Q. Li, L. Liu, D. Mao, Y. Yu, W. Li, X. Zhao and C. Mao, *J. Am. Chem. Soc.*, 2020, **142**, 665–668.
34 D. Sun, Z. Luo, J. Lu, S. Zhang, T. Che, Z. Chen and L. Zhang, *Biosens. Bioelectron.*, 2019, **134**, 49–56.
35 A. Qu, X. Wu, S. Li, M. Sun, L. Xu, H. Kuang and C. Xu, *Adv. Mater.*, 2020, **32**, 2000184.
36 Z. Luo, D. Sun, Y. Tong, Y. Zhong and Z. Chen, *Microchim. Acta*, 2019, **186**, 374.
37 M. Dadashi Firouzjaei, M. Karimiziarani, H. Moradkhani, M. Elliott and B. Anasori, *Mater. Today Adv.*, 2022, **13**, 100202.
38 C. Zhang, *J. Energy Chem.*, 2021, **60**, 417–434.
39 Z. Qin, H. Deng, R. Huang and S. Tong, *Chem. Eng. J.*, 2022, **428**, 132493.
40 M. F. Huang, Y. C. Kuo, C. C. Huang and H. T. Chang, *Anal. Chem.*, 2004, **76**, 192–196.
41 B.-C. Luo, L.-Y. Yuan, Z.-F. Chai, W.-Q. Shi and Q. Tang, *J. Radioanal. Nucl. Chem.*, 2015, **307**, 269–276.
42 D. Song, X. Jiang, Y. Li, X. Lu, S. Luan, Y. Wang, Y. Li and F. Gao, *J. Hazard. Mater.*, 2019, **373**, 367–376.
43 D.-L. Li, X. Zhang, Y. Ma, Y. Deng, R. Hu and Y. Yang, *Anal. Methods*, 2018, **10**, 3273–3279.
44 H. R. Abid, J. Shang, H. M. Ang and S. Wang, *Int. J. Smart Nano Mater.*, 2012, **4**, 1–11.
45 F. Petraki, V. Papaefthimiou and S. Kennou, *Org. Electron.*, 2007, **8**, 522–528.
46 M. Adeel, M. M. Rahman and J. J. Lee, *Biosens. Bioelectron.*, 2019, **126**, 143–150.
47 N. S. Lopa, M. M. Rahman, F. Ahmed, T. Ryu, S. C. Sutradhar, J. Lei, J. Kim, D. H. Kim, Y. H. Lee and W. Kim, *Biosens. Bioelectron.*, 2019, **126**, 381–388.
48 Y. Ding, H. Shang, X. Wang and L. Chen, *Analyst*, 2020, **145**, 6079–6084.
49 X. Lin, C. Li, C. He, Y. Zhou, Z. Wang, N. Duan and S. Wu, *ACS Appl. Nano Mater.*, 2021, **4**, 8231–8240.
50 Y. Ding, H. Shang, X. Wang and L. Chen, *Analyst*, 2020, **145**, 6079–6084.
51 R. Huang, L. L. Xiong, H. H. Chai, J. J. Fu, Z. Lu and L. Yu, *RSC Adv.*, 2019, **9**, 38590–38596.
52 J. Xu, W. Li, R. Liu, Y. Yang, Q. Lin, J. Xu, P. Shen, Q. Zheng, Y. Zhang, Z. Han, J. Li and T. Zheng, *Sens. Actuators, B*, 2016, **232**, 577–584.
53 X.-L. Yan, X.-X. Xue, J. Luo, Y.-T. Jian, L. Tong and X.-J. Zheng, *Sens. Actuators, B*, 2020, **320**, 128375.
54 W. Yuan, L. Lu, Y. Lu, X. Xiong, Y. Li, X. Cui, Y. Liu and X. Xiong, *Food Anal. Methods*, 2021, **14**, 2308–2316.